Thermopower probing emergent local moments in magic-angle twisted bilayer graphene

Ayan Ghosh[1,*], Souvik Chakraborty[1,†], Ranit Dutta[1,‡], Adhip Agarwala[2], K. Watanabe[3], T. Taniguchi[3], Sumilan Banerjee[1], Nandini Trivedi[4], Subroto Mukerjee[1] and Anindya Das[1,§]

[1] *Department of Physics, Indian Institute of Science, Bangalore, 560012, India.*
[2] *Indian Institute of Technology Kanpur, Kalyanpur, Uttar Pradesh 208016, India*
[3] *National Institute for Materials Science, 1-1 Namiki, Tsukuba 305-0044, Japan.*
[4] *Department of Physics, The Ohio State University, Columbus, Ohio - 43210, USA.*

[*] equally contributed
[†] equally contributed
[‡] equally contributed
[§] anindya@iisc.ac.in

SI-1: Device fabrication.

We have employed the modified "tear and stack" [1] technique to fabricate the twisted heterostructures. First, on Si/SiO_2 substrates, hBN and graphene are separately exfoliated. Then, suitable flakes are sorted for fabrication. Suitable single larger graphene flakes are then pre-cut to form into two, to be picked up sequentially. hBN, with thickness between $\sim 10nm - 25nm$ are commonly used for encapsulation. A film of transparent poly propyl carbonate (PPC) on top of a hemispherical PDMS stamp is used to pick up the top hBN layer. Using this PDMS-PPC-hBN stamp, we pick up the pre-cut graphene (mono/bi) layers, one after the other, while introducing a rotation between subsequent pick-ups to introduce the desired twist angle. Finally, another hBN flake is picked up, which encapsulates the TBLG/TDBLG layers. The whole stack is then placed on a clean Si/SiO_2 substrate. During the whole stack-making process, a temperature at or below 55^o C is maintained to reduce the chances of thermal relaxation of the twist angle. The final landing on Si/SiO_2 substrate is also done at 75^o C for the aforementioned reason.

To make the 1D edge contacts, we spin-coat with 495A4-950A4 PMMA bilayer, which acts as a negative resist. Unlike the shorter duration of usual 180^oC baking, each PMMA layer was baked at 80-100^oC for 15 minutes to avoid thermal relaxation of the introduced twist angle. Then, the contacts, including a thin heater line, are defined using standard e-beam lithography (EBL), with the dose optimized for low baking temperature of PMMA. Following the lithography, contacts are etched with CHF_3-O_2 plasma followed by thermal deposition of $Cr(2nm)$, $Pd(10nm)$ and $Au(70nm)$. The width of source and drain contacts on all devices are $\sim 1\mu m$, while the heater lines are $\sim 200 - 300nm$ in width. The heater lines are separated by around $3\mu m$ gap from the source contacts. Additionally, for the dual-gated near magic-angle twisted bilayer graphene (MATBLG) device, after the 1D edge contacts are deposited, we define the area of the top gate by EBL, followed by depositing Cr/ Au (5 nm/ 70 nm) in the defined region over the top hBN. The Si/SiO_2 substrate acts as a back gate for all three devices. Finally, the channel geometry is mapped out by EBL, and the rest of the graphene domains are etched out to define the channel geometry. Optical images of the measured devices, i.e., MATBLG, near MATBLG, and twisted double bilayer graphene (TDBLG), are presented in Extended Data Fig. 1a, b, and c insets, respectively.

SI-2: Thermopower measurement scheme:

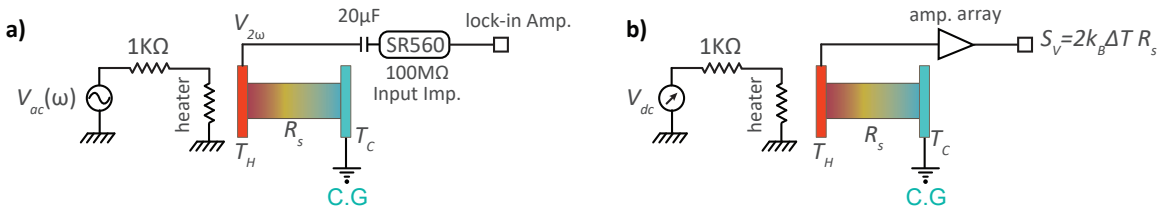

SI-Fig. 1: Thermoelectric Voltage (V_{Th}) measurement scheme. (a) A current is passed through the heater to create the temperature gradient across the sample. The thermoelectric voltage was measured using standard $V_{2\omega}$ method. **(b)** Johnson noise thermometry to measure the temperature difference between the source and drain.

Thermoelectric voltage (V_{Th}) measurement: A simplified V_{Th} measurement scheme is shown in SI-Fig. 1a. We inject ac (I_h) through the heater line at 7 Hz (via a $1k\Omega$ resistance connected in series to the heater line acting as the ballast resistance). The V_{Th} is measured across the source and drain contacts as the

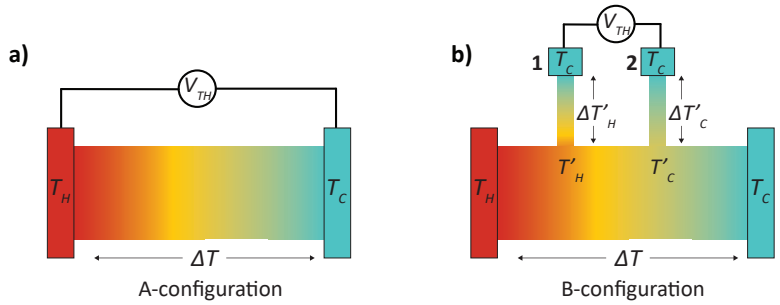

SI-Fig. 2: Temperature profile and thermoelectric voltage measurement in different geometry: (a) and **(b)**, respectively, show the temperature profile across the measurement leads for 2-probe, A-configuration and 4-probe, B-configuration.

second harmonic (14 Hz) Y-component ($V_{2\omega}$) signal generated across the sample, which is measured via the lock-in using a 100-gain amplifier (SR-560). The drain probe (i.e., the farthest device contact from the heater) is directly bonded to the cold finger; this thermally anchors the drain to the MC plate of the dilution refrigerator, which serves as a cold ground (C.G).

For V_{Th} measurement, one has to be mindful of stray components of thermoelectric voltage emerging from temperature gradients between the measurement probes and sample which can potentially render the V_{Th} measurement inaccurate. In following segment, we discuss various inaccuracies that may or may not influence the V_{Th} measurement depending on the measurement scheme.

In SI-Fig 2, in a cartoon diagram, we highlight the temperature gradients (as color gradient) across the sample as well as the probes that comprise the measured V_{Th} for a 2-probe as well as a 4-probe geometry. While a 4-probe geometry is ubiquitous for negating contact-resistance effects for R_{xx} measurement, the same is not entirely true for measuring the longitudinal component of thermoelectric voltage V_{Th}^{xx}. Therefore, it is not accurate to label V_{Th} in 2-probe or 4-probe geometry, rather we will address them as V_{Th} in A-configuration or B-configuration, respectively. However, in practice, a B-configuration geometry is arguably complicated for V_{Th} measurement, as many stray components of temperature gradients across the measurement probes also get included in the measured V_{Th}. Referring to SI-Fig 2b, (because of the large metal effectively acting as a temperature bath), the metal leads at contacts 1 and 2 essentially maintain the bath temperature T_C or very close to that. However, the thin probes connecting the channel to the metal leads do experience temperature variations. For probe 1 (2), the temperature difference is $\Delta T'_H = T'_H - T_C$ ($\Delta T'_C = T'_C - T_C$), T'_H (T'_C) being local the temperature of the channel at the position of probe 1 (2). These will introduce stray components of thermoelectric voltage in series to the measurement circuit. Hence the measured V_{Th} will have the following components-

$$V_{Th}^{4-probe} = -V_{Th}^{\Delta T'_H} + V_{Th}^{T'_H - T'_C} + V_{Th}^{\Delta T'_C} \tag{1}$$

Where, $-V_{Th}^{\Delta T'_H}$ comes from temperature gradient across probe 1 (note the $-ve$ sign is considered since, because of the temperature gradient direction, $V_{Th}^{\Delta T'_H}$ will oppose rest of the thermoelectric components). Similarly, $V_{Th}^{\Delta T'_C}$ and $V_{Th}^{T'_H - T'_C}$ are the components coming from probe 2 and the channel (between probe 1 and 2), respectively. Even in a simplified assumption that both the probes have an identical material compo-

sition and geometry (i.e, identical thermoelectric properties), $V_{Th}^{\Delta T'_H} \neq V_{Th}^{\Delta T'C}$ since $\Delta T'_H \neq \Delta T'_C$, which depends on various details like the temperature profile created by the heater and, the thermal conductivity of the metals/substrates etc. Thus unlike R_{xx} measurement where we nullify contact effects by (open circuit voltage measurement), $V_{Th}^{4-probe}$ will have non-negligible influences of the probes. In practice, these probe contributions can be significant as they rarely are identical (due to strain or being of a different composition than the channel or because of the inaccuracies of fabrication etc). On the other hand, none of these aforementioned components are present in A-configuration geometry. Note that the interfaces generally are also a contributor to thermoelectric voltage in both A-configuration and B-configuration geometry, but between the probes and metal leads the interfaces are effectively one-dimensional, thus temperature drop across the interfaces (ΔT) can be neglected, hence having negligible contribution in thermoelectric voltage. In our measurement, we have utilized A-configuration for measuring V_{Th} for the three devices. Note that, for near MATBLG device, which has a Hall-geometry, the V_{Th} measurement has been performed between the extreme two contacts (i.e. equivalent to configuration-A).

Temperature gradient measurement scheme with noise thermometry: We have employed Johnson noise thermometry to measure the temperature difference, ΔT, at lower temperatures below $10K$ as shown in SI-Fig. 1b. For this measurement, equivalent dc current is sent through the heater line to create the temperature gradient across the sample, and thermal noise is measured using a LC-resonant circuit. The details can be found in our earlier work [2, 3]. In the absence of any heater current, the sample temperature maintains equilibrium with the MC plate temperature of the dilution refrigerator via cold ground. In this case, measured thermal noise is given by ${S_V}^0 = 4k_BT_cR_s$, where T_c is the temperature of the MC plate of the dilution refrigerator and R_s refers to the sample resistance between the cold ground and the hot contact. In the presence of finite heater current, the thermal noise will rise to ${S_V}^{Av} = 4k_BT_{Av}R_s$ due to the average temperature T_{Av} of the device being higher than T_c. Due to the applied temperature gradient, the excess thermal noise is given by $\Delta S_V = {S_V}^{Av} - {S_V}^0 = 2k_B\Delta TR_s$ [2, 3]. A detailed derivation of this expression is provided in our earlier works [2, 3]. Note that, at temperatures beyond $10K$, ΔT calculation by noise thermometry does not remain as accurate as at lower temperatures. Extracting the excess noise over the already high background noise, although not impossible, is challenging as it requires noise data acquisition over a significantly extended time. In the main manuscript, since we only concentrate on the sign changes and relative amplitude of the thermopower data, we present only the thermoelectric voltage V_{Th} except, the data at $8K$ is converted to thermopower and shown in Extended Data Fig. 2c, and the magnitudes are of the order of $\sim 8\mu$V/K at low temperatures.

Measuring thermoelectric voltage in linear response regime: In the top panel of Extended Data Fig. 2a andExtended Data Fig. 2d, we show the measured $V_{2\omega}$ signal versus back gate voltage (V_{bg}) at a few different applied heater currents for MATBLG device, at temperature $8K$ and $40K$, respectively. Extended Data Fig. 2a,d-bottom panels show the same thermoelectric voltages normalized with respective heater current squared (I_h^2). All the normalized $V_{2\omega}/I_h^2$ values overlap well, since the Joule heating, and hence, the temperature difference is proportional to I_h^2. This shows the $V_{2\omega}$ measurements have been performed in the linear response regime. Further, the extracted ΔT from the thermal noise measurement is shown as a function of I_h^2 in Extended Data Fig. 2b. Within the maximum heater current range, a clear linear trend (dashed red line) can be observed between ΔT and I_h^2, and $\Delta T << T$. Finally, Extended Data Fig. 2c shows the thermopower calculated from $V_{2\omega}$ signal and ΔT data, and around $10K$ its magnitude is of the order of $\sim 8\mu V/K$. We have measured all the thermoelectric voltages for different temperatures in the linear regime by making sure that the normalized thermoelectric voltages ($V_{2\omega}/I_h^2$) collapses to a single

curve similar to Extended Data Fig. 2a-bottom panel. Extended Data Fig. 2e shows the same linearity check performed in TDBLG device.

SI-3: Comparison with the Mott formula:

The semi-classical equation (described in Eq.1 in the Methods section) can be further simplified using the Somerfeld approximation to Mott's formula as;

$$S_{Mott} = -\frac{\pi^2 k_B^2 T}{3e} g(\epsilon)_{\epsilon=\epsilon_f} \frac{dln(R)}{dn}, \tag{2}$$

According to Eq. 2, the term $dln(R)/dn$ is responsible for sign changes observed in Mott-thermopower (S_{Mott}). To know whether the Mott relation is valid, we will compare the experimentally measured (V_{Th}) and the Mott thermopower using $dln(R)/dn$. We present a detailed comparison of V_{Th} and $dln(R)/dn$ as a function of filling ν at different temperature ranges for the three representative devices in Extended Data Fig. 5,6.

SI-4: Theoretical section for thermopower from atomic orbital physics:

The experimental data for the thermoelectric voltage, V_{Th} is shown in Figure. 2 and Figure. 5 in the main text. It shows a distinct evolution from the high-temperature limit where it can be described as arising from effective graphene bands. As the temperature is lowered to the scale of the f-electrons bandwidth, the behavior changes. In particular, from a single crossing where the sign of thermopower changes just at $\nu = 0$ to three crossings where additional crossing appears near $\nu \sim \pm 1$. We show below that the presence of local moments that can emerge from the narrow f-bands can qualitatively explain several of the experimental features of the thermopower, in particular: (i) Appearance of the additional crossings. (ii) The stability of the value of crossing with reducing temperature.

It is useful to identify the different energy scales associated with the system. (i) The bandwidth of the flatband $\equiv W(\sim 5 - 10meV)$, (ii) the Hubbard interaction strength ($U \sim 20meV$), (iii) gap between the dispersing lower and upper bands ($\Delta_g \sim 30meV$). The different energy scales are shown below.

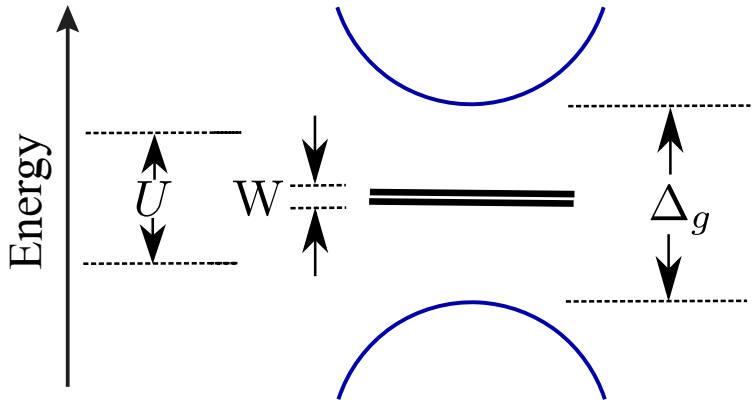

$T > \Delta_g$: The high-temperature thermopower is positive for $\nu < 0$ and negative for $\nu > 0$ (as depicted in the 1st row of Extended Data Fig. 8). This is characteristic of graphene-based systems where electron-hole symmetry renders one crossing at $\nu = 0$ and with respect to this Dirac point, hole (electron) based carriers lead to positive (negative) thermopower for $\nu < 0 (> 0)$ [4].

$U < k_B T \approx \Delta_g$: As the temperature falls below Δ_g, the behavior of the thermopower flips to being negative for $\nu < 0$ and positive for $\nu > 0$. In this regime, the excitations on the scale of Δ_g are suppressed, and the effect of flat bands becomes observable.

$U \approx k_B T < \Delta_g$: In this regime, the effect of the flatbands dominates, in particular the emergent local moments due to strong Coulomb repulsion. To capture the atomic limit, we consider four orbitals per site, with negligible hopping between sites. The filling of these orbitals dominates the physics between $-4 < \nu < 4$. For $K_B T \sim U$, we see a single crossing at $\nu = 0$. In this regime, we have an equal likelihood of $|0\rangle, |\uparrow\rangle, |\downarrow\rangle, |\uparrow\downarrow\rangle$ of all four states. This leads to entropy being maximum at $\nu = 0$ and single thermopower crossing at $\nu = 0$. This also gets captured in Extended Data Fig. 9a,b when $U \lesssim k_B T < \Delta_g$ (effectively non-interacting regime) and shown by the 3rd row of the Extended Data Fig. 8. However, at a slightly higher temperature range, $U < k_B T \approx \Delta_g$, both the contributions from the 1st row and 3rd row of the Extended Data Fig. 8 can be significant, and result in almost flat near zero thermoelectric voltage (as shown by the 2nd row in Extended Data Fig. 8).

$k_B T < U$: In this low-temperature regime, we find a qualitatively new feature where three prominent crossings appear (last row of Table 1). As we discuss below, this is dominantly due to interactions which changes the entropic contributions to thermopower.

From the experiment, three qualitatively distinct regimes are clearly identified, 1st row, 2nd row, and last row of Table 1. However, the 3rd row of Table 1 is seen in the experiment only around $70K$, as shown in Figure. 5b of the manuscript. The last column of Extended Data Fig. 8 shows the corresponding experimental plots.

Details about entropy calculations: The Hamiltonian in the atomic limit is given by

$$H = \sum_{\alpha} \left(U n_{\alpha\uparrow} n_{\alpha\downarrow} + \epsilon_\alpha n_\alpha \right) \tag{3}$$

where $\alpha = \{1, \ldots, 4\}$ labels the four orbitals and U is the Hubbard interaction. Upon evaluating the partition function Z, we obtain the corresponding Helmholtz free energy $F = -k_B T \log Z$ and from that the entropy $S = -\left(\frac{\partial F}{\partial T}\right)$.

The thermopower is then given by (using the Kelvin formula),

$$S_e = -\frac{1}{e} \frac{\partial S}{\partial \rho} \tag{4}$$

where e is electric charge[5]. It is to be noted that μ is solved self-consistently to fix the number density ρ. In strongly interacting systems, particularly when electronic bandwidth is comparatively smaller to temperature and/or interactions, interpretation of thermopower when analysed in atomic limit has met remarkable

success. In particular it has been useful to explain its non-monotonic behavior (as a function of temperature) in strongly correlated systems[6, 7, 8], their magnetic field dependence [9] and predict characteristic zero crossings of thermopower as a function of density where effective phase space gets modified due to strong interactions. [10]. The recurring idea here is that at large temperatures, even in presence of strong interactions, the thermopower is essentially how *thermodynamic entropy* changes with variations in carrier density [11]. Given bilayer graphene at magic angles has a flat band and comparatively strong interactions [12, 13, 14, 15] – we explore this limit of analysis in context of the experimental data. Assuming $-\epsilon_1 = -\epsilon_2 = \epsilon_3 = \epsilon_4 = 0.2meV$ we investigate the behavior of thermopower as a function of temperature and Hubbard interaction strength $U_\alpha = U$ which is kept same for all the orbitals. The resulting behavior is shown in Extended Data Fig. 9c,d.

While in absence of any interactions the thermopower shows a single crossing at $\nu = 0$ with increasing temperature. This single crossing happens here since the entropy maximizes exactly at $\nu = 0$. This is essentially the point where the phase space is maximum given both the particles and holes are equal. However as interactions are slowly increased, a characteristic undulation develops near $\nu = 0$ which creates two extra crossings which remain stable even at relatively large high temperatures. These interaction dominated crossings develops at $\nu = \pm\frac{4}{3}$. Even for a single orbital model, given N_A atoms and N electrons in the system, the total number of states are [10]

$$g = \frac{N_A! 2^N}{N!(N_A - N)!} \tag{5}$$

In thermodynamic limit this gives the thermopower as $S \sim \frac{d \log g}{d\rho} \sim \log(2(1-\rho)/\rho)$, thus giving a zero crossing at $\rho = \frac{2}{3}$. This corresponds to for the four orbital model $\nu = 4(\rho - 1) = -\frac{4}{3}$. This is strikingly similar to the experimental observations at high temperatures which seems to point out that even at high-temperatures strong correlation physics is at play in the twisted bilayer graphene system. A similar calculation taking into account doublons will lead to a crossing near $\nu = \frac{4}{3}$. Expanding the orbital energies such that $-\epsilon_1 = -\epsilon_4 = 5meV$ $-\epsilon_3 = \epsilon_4 = 1.7meV$ and with a Hubbard interaction of around $25meV$ we again find that the extra crossings appear for $T < 100K$ (see Fig. 3) however now closer to $\nu \sim \pm 1.1$. This reflects that atomic orbital limit captures the essential experimental phenomenology of thermopower in the magic angle twisted bilayer graphene.

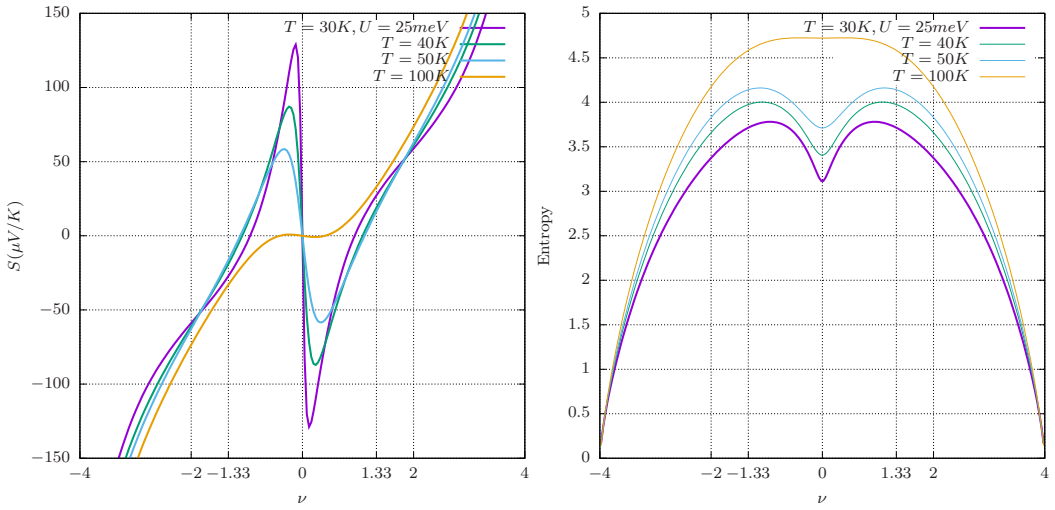

SI-Fig. 3: Behavior of entropy and thermopower for the four orbital atomic limit where the onsite energies are $-\epsilon_1 = -\epsilon_4 = 5meV$ $-\epsilon_3 = \epsilon_4 = 1.7meV$, Hubbard interaction $U = 25meV$ as a function of filling.

References

1. Cao, Y. *et al.* Unconventional superconductivity in magic-angle graphene superlattices. *Nature* **556**, 43–50 (2018).

2. Paul, A. K. *et al.* Interaction-driven giant thermopower in magic-angle twisted bilayer graphene. *Nature Physics* 1–8 (2022).

3. Ghosh, A. *et al.* Evidence of compensated semimetal with electronic correlations at charge neutrality of twisted double bilayer graphene. *Communications Physics* **6**, 360 (2023).

4. Zuev, Y. M., Chang, W. & Kim, P. Thermoelectric and magnetothermoelectric transport measurements of graphene. *Phys. Rev. Lett.* **102**, 096807 (2009). URL https://link.aps.org/doi/10.1103/PhysRevLett.102.096807.

5. Peterson, M. R. & Shastry, B. S. Kelvin formula for thermopower. *Phys. Rev. B* **82**, 195105 (2010). URL https://link.aps.org/doi/10.1103/PhysRevB.82.195105.

6. Beni, G. Thermoelectric power of the narrow-band hubbard chain at arbitrary electron density: Atomic limit. *Phys. Rev. B* **10**, 2186–2189 (1974). URL https://link.aps.org/doi/10.1103/PhysRevB.10.2186.

7. Mukerjee, S. Thermopower of the hubbard model: Effects of multiple orbitals and magnetic fields in the atomic limit. *Phys. Rev. B* **72**, 195109 (2005). URL https://link.aps.org/doi/10.1103/PhysRevB.72.195109.

8. Koshibae, W., Tsutsui, K. & Maekawa, S. Thermopower in cobalt oxides. *Phys. Rev. B* **62**, 6869–6872 (2000). URL https://link.aps.org/doi/10.1103/PhysRevB.62.6869.

9. Mukerjee, S. & Moore, J. E. Doping dependence of thermopower and thermoelectricity in strongly correlated materials. *Applied physics letters* **90**, 112107 (2007).

10. Chaikin, P. M. & Beni, G. Thermopower in the correlated hopping regime. *Phys. Rev. B* **13**, 647–651 (1976). URL https://link.aps.org/doi/10.1103/PhysRevB.13.647.

11. Shastry, B. S. Thermopower in correlated systems. In *New Materials for Thermoelectric Applications: Theory and Experiment*, 25–29 (Springer, 2013).

12. Bistritzer, R. & MacDonald, A. H. Moiré bands in twisted double-layer graphene. *Proceedings of the National Academy of Sciences* **108**, 12233–12237 (2011).

13. Koshino, M. *et al.* Maximally localized wannier orbitals and the extended hubbard model for twisted bilayer graphene. *Phys. Rev. X* **8**, 031087 (2018). URL https://link.aps.org/doi/10.1103/PhysRevX.8.031087.

14. Kang, J. & Vafek, O. Symmetry, maximally localized wannier states, and a low-energy model for twisted bilayer graphene narrow bands. *Phys. Rev. X* **8**, 031088 (2018). URL https://link.aps.org/doi/10.1103/PhysRevX.8.031088.

15. Po, H. C., Zou, L., Vishwanath, A. & Senthil, T. Origin of mott insulating behavior and superconductivity in twisted bilayer graphene. *Phys. Rev. X* **8**, 031089 (2018). URL https://link.aps.org/doi/10.1103/PhysRevX.8.031089.